SUPPLEMENTARY INFORMATION

1. Device fabrication and characterization

Our fabrication process is discussed in four sections: wire fabrication, molecular deposition, electromigration, and characterization.

Wire fabrication

The device fabrication consists of four lithographic steps. In the first step, contact pads are defined by evaporation of 3 nm Ti and 150 nm Au. Secondly, the aluminum gate electrode is defined (2 μm wide and 15 nm thick). The sample is then taken out of the vacuum chamber of the evaporator and placed into a desiccator filled with oxygen to grow an insulating oxide. The native aluminum oxide is typically 3 nm thick. This localized-bottom aluminum gate electrode with a thin dielectric layer (Al_2O_3) provides more efficient gate coupling than the more often used approach of a back-gate configured silicon wafer (a highly doped silicon wafer back-gate, with a top silicon oxide). The third step involves the definition of the thin and narrow gold wire that will be broken by electromigration. A 15 nm thick and typically 100 nm wide gold wire is evaporated on the region over the aluminum gate electrode. In the last step, the thin gold wire is connected to the contact pads by evaporation of 3 nm thick Ti and 100 nm thick Au. The first step of making contact pads was performed by photolithography, and other steps were performed by electron-beam lithography. Scanning electron microscopy (SEM) images of the fabricated device are shown in the inset of Fig. 1a (active part) and Fig. S1 (full pattern).

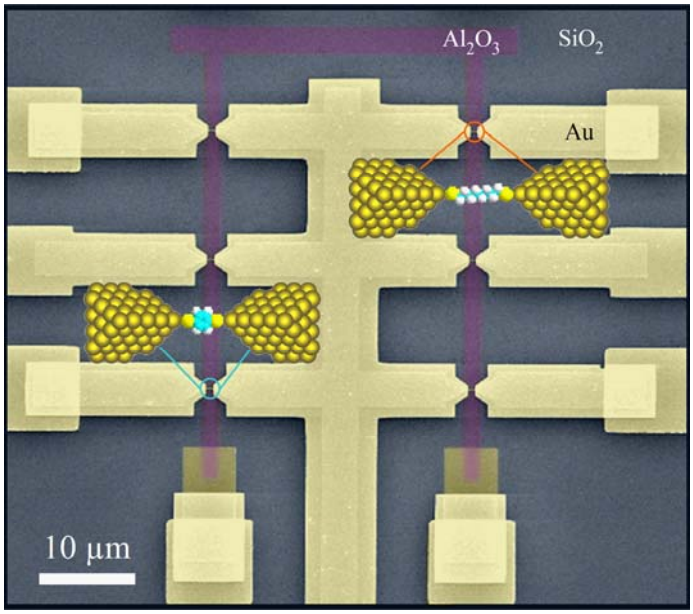

Figure S1. Scanning electron microscope image (false color) illustrating a full pattern of the devices. The whole structure was defined on an oxidised Si wafer. The yellow regions show portions of the multi-layered Au electrodes (a thin Au layer with a thickness of ~15 nm; a thick Au layer with a thickness of ~100 nm), and the purple region represents the oxidised Al gate electrode. Au wires broken by the electromigration technique (Fig. 1a, inset) are placed on the top of the bottom-gate electrode. The contact pads to which a connection is made by wire bonding are not visible because they are located far from the active part of the device. Insets display the schematic images of Au-ODT-Au (right) and Au-BDT-Au (left) junctions. This is a conceptual diagram only, as only one molecular junction type at a time can be fabricated with the present process.

Molecular deposition

After cleaning in oxygen plasma for 1 min, the samples were immersed in a dilute solution (1 mM) of ODT and BDT in 10 mL ethanol for 24 h. The molecular deposition was done on the gold surface in the solution inside a nitrogen-filled glove box with an oxygen level less than 10 ppm. The molecules self-assemble onto the gold wires by the thiol-gold linkage[S1]. Before use, each sample is rinsed in ethanol and gently blown dry in a nitrogen stream.

Electromigration: Nanogap fabrication

Thereafter, the samples coated with the molecules were immediately cooled to 4.2 K (in a vacuum cryostat), and the electromigration-induced breakage was performed. It has been shown[S2] that nanometre-scale gaps in small metal wires can be formed by increasing a d.c. voltage across the wire until a substantial increase in the resistance is observed, at which point the applied voltage is rapidly reset to zero. This method was used here, with the procedure repeated to reach a target resistance corresponding to a molecular-sized tunnelling gap (normally greater than several MΩ). Figure S2 shows typical $I(V)$ curves during breaking of the metal wire. In the first $I(V)$ scan, the current starts to decrease at 0.8 V. In the second and third $I(V)$ scans, one observes a gradual decrease (increase) in the current (resistance) of the metal wire, resulting from the electromigration. In the final $I(V)$ scan, it is seen that the current abruptly decreases (as pointed by an arrow), and the metal wire is completely broken to form a nanometer-scale separation between the disconnected metal wires, across which individual molecules can be often bridged.

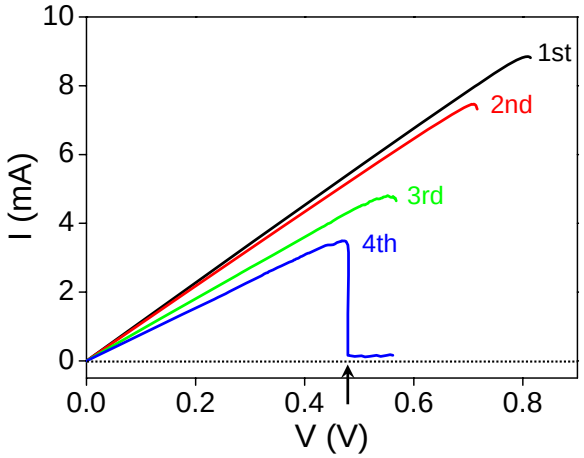

Figure S2. *I*(*V*) curves while breaking metal wire.

Figure S3 shows high resolution SEM images of the gold wires broken by the electromigration. These figures clearly show that the gap size at the narrowest point is less than 2 nm, similar to the molecular length scale we need to achieve. Similar results have been obtained and imaged by other groups (there are publications that show TEM images of the 1-2 nm broken gaps)[S3].

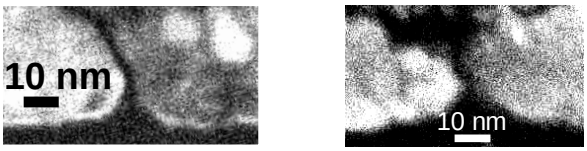

Figure S3. High resolution SEM images of a gold wire broken by electromigration.

Characterization

In the process of breaking the wire, the molecules covering the surface of the initial wire occasionally become trapped in the junction (with random orientations). The molecular

trapping events between the separated gap electrodes are not controllable, but inherently stochastic. The success rate for observing a characteristic that indicates a molecular junction is typically less than 10%. Our yield (35/418) for 'working devices' is consistent with other results[S4]. We note that there are many that have no molecule, or perhaps many, or bad orientations, etc. – this fabrication is a probabilistic process. When they do work (which we show in this characterization section), the community has established criteria by which they constitute single or few molecule junctions.

Conductance — It is important to notice that the measured conductance is consistently and repeatedly dependent on the molecular species, and in agreement with literature:

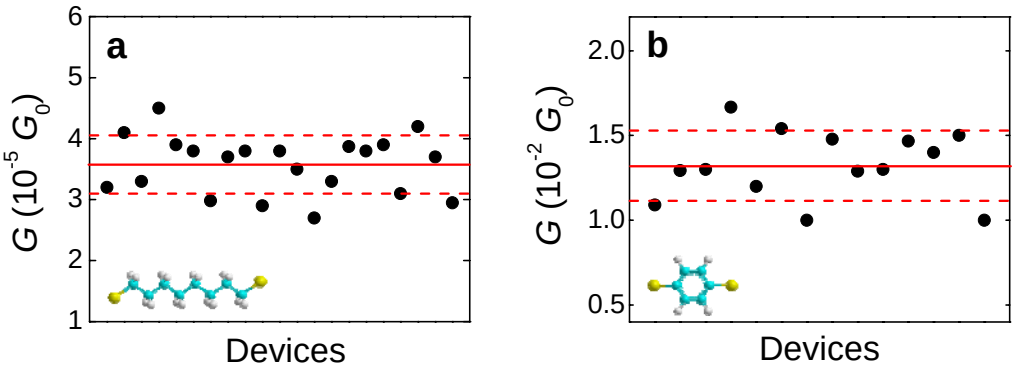

Figure S4. Low-bias (0–0.1 V) conductance values (G) measured at V_G = 0 V from the 35 working devices of **a,** the ODT (21 devices) and **b,** BDT (14 devices) junctions. The solid lines represent the mean conductance, and the dashed lines show the standard deviation of the measurements. The mean conductance with the standard deviation (m ± σ) was calculated to be (3.57 ± 0.48) × 10^{-5} G_0 (= $2e^2/h$) for ODT and (1.32 ± 0.21) × 10^{-2} G_0 for BDT, which is in good agreement with single molecule conductance values of ODT and BDT molecules in previous reports[S5]. Our devices are in agreement with a considerable literature on similar single molecule transport, and thus we conclude that there is a single molecule, (or very few molecules, reproducibly) in the electromigrated molecular junctions.

Temperature-variable current-voltage measurement — The temperature independent $I(V)$ characteristic is an important verification of tunnelling, and eliminates many of the other potential alternative mechanisms:

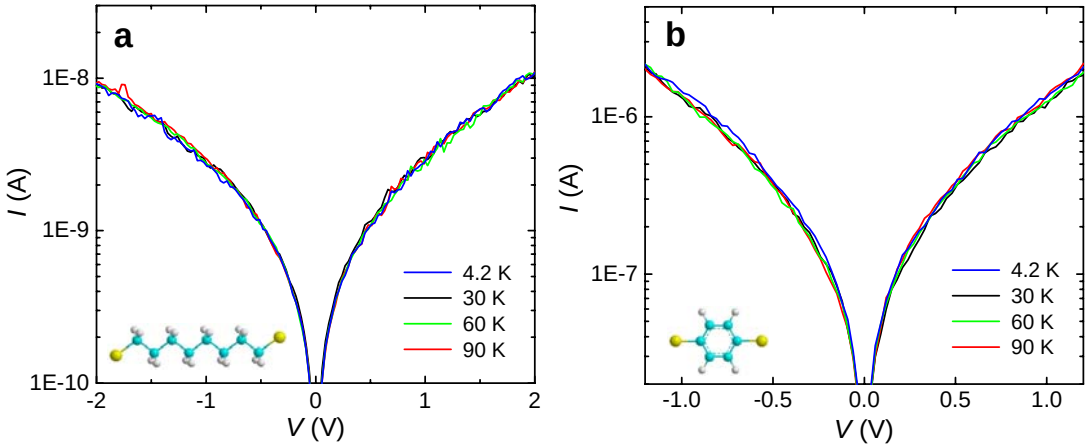

Figure S5. Semilog plots of temperature-variable $I(V)$ data for **a,** Au-ODT-Au and **b,** Au-BDT-Au junctions measured at selected temperatures (4.2, 30, 60, and 90 K). No temperature dependence of the $I(V)$ curves was observed, which confirms that tunnelling is the main conduction mechanism for these junctions in the bias and temperature range measured. The off-resonant tunnelling mechanism can be reasonably expected because the Fermi energy of the electrode lies deep within the large HOMO-LUMO gap of the short molecules.

Length-dependent tunnelling transport — An important characterization method that validates molecular tunnelling transport is the exponential decrease of conductance on the molecular length. A correct exponential dependence, temperature dependence, and agreement with decay coefficients all point to a valid molecular junction. We measured the conductance of two other alkanedithiols, 1,6-hexanedithiol [HS-$(CH_2)_6$-SH, denoted as HDT] and 1,10-decanedithiol [HS-$(CH_2)_{10}$-SH, DDT], to study the dependence of the

conductance on molecular length. The conductance of alkanedithiol molecules is expected to show an exponential decrease with molecular length. In particular, the conductance G is expected to be proportional to $\exp(-\beta N)$, where N is the number of carbon atoms in the alkanedithiol and β is the tunnelling decay coefficient:

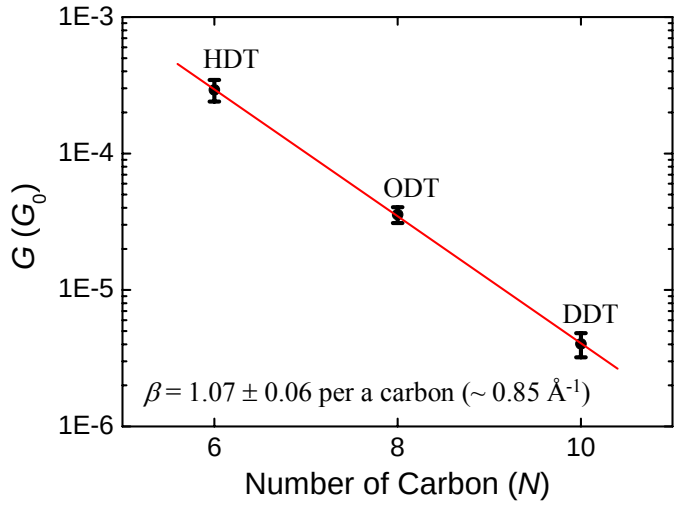

Figure S6. Semilog plot of the conductance versus the length of molecules for the three different length alkanedithiol junctions (all made from the electromigration-induced break junction), which can be used to obtain the tunnelling decay coefficient β. We found β = 1.07 per carbon atom (or ~0.85 Å^{-1}). This β value is in excellent agreement with the literature for tunnelling transport through the aliphatic alkyl chains[S6].

Inelastic electron tunnelling (IET) spectroscopy — Recently, IET spectroscopy has become a primary tool for molecular identification in molecular junctions[S7], analogous to IR and Raman spectroscopy for macroscopic samples, for an unambiguous determination of the molecular species in the junction. We measured fully assigned IET spectra for ODT and BDT junctions (Figs. 3a and 4a in main text). All of the spectral features are attributable to vibrational modes associated with the molecular species,

which implies that the molecule is the only thing in the junction through which tunnelling is occurring.

The characterization methods described here are generally accepted by the community as evidence of a single-molecule junction. However, these are in some sense “indirect”, in that the specific molecule for which transport is occurring is not spatially imaged. This is an outstanding challenge of the field. However, at present a single-molecule junction appears to be the best consistent interpretation of the data presented here and similarly elsewhere.

2. Transfer characteristics of a 1,4-benzenedithiol molecular transistor

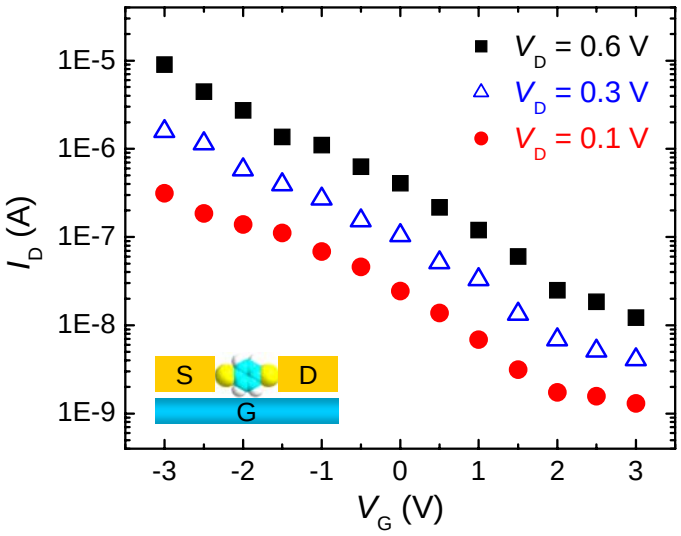

Figure S7. Transfer characteristics of a 1,4-benzenedithiol molecular transistor − i.e., semilog plots of drain current I_D versus gate voltage V_G at drain biases V_D of 0.1, 0.3, and 0.6 V. The tunnelling current is enhanced with a negative V_G, while a positive V_G suppresses the current level, indicative of a p-type transistor.

3. Low temperature transport and IET spectroscopy measurements

Low temperature transport measurements

Transport measurements of the electromigrated molecular junctions were performed with a custom-built cryogenic measurement apparatus. The devices are mounted onto a 28-pin leadless chip carrier socket on the sample stage inside a vacuum chamber that is evacuated and purged with He gas before being lowered into a liquid He storage dewar. All the electromigration break processes and transport measurements were made at liquid He temperature (4.2 K). In order to reduce the noise level, triaxial cables are used to connect the socket leads to the measurement instruments outside the cryogenic vacuum chamber through vacuum electrical feedthroughs. A calibrated Lakeshore thermometer is mounted on the sample stage to monitor sample temperature, and a resistive heater in a feedback loop with the thermometer is mounted on the sample stage to maintain the sample temperature. In order to measure the $I(V)$ characteristics, we used a 16-bit DAC for bias voltages, and a low-noise current amplifier (Ithaco 1211) followed by a DMM (Agilent 34410) for current measurement. All the grounds of system are isolated to remove ground-loops and electrical noise. The sweep rate of source-drain voltage for a given gate voltage was ~1 V/min for normal $I(V)$ sweeps and 0.1−0.05 V/min for IET spectroscopy sweeps. The sweeps were checked for hysteresis for both directions and polarities; none was found.

IET spectroscopy measurements

All of the $\mathrm{d}I/\mathrm{d}V$ and $\mathrm{d}^2I/\mathrm{d}V^2$ data were directly measured at 4.2 K using a lock-in amplifier (Stanford Research Systems 830) and a homebuilt current–voltage sweeper

controlled by a computer running via GPIB. An a.c. modulation of 7.8 mV (root-mean-square) at a frequency of 1,033 Hz with time constant of 1s was applied to the sample to obtain the first and second harmonic signals, proportional to dI/dV and d^2I/dV^2, respectively. The a.c. modulation is added to a d.c. bias generated by a battery-powered 16-bit DAC converter, using operational amplifier-based custom circuitry[S8]. The obtained lock-in signals were checked by agreement between repeated measurements. Finally, the IET spectra are presented as the normalised amplitude, $(d^2I/dV^2)/(dI/dV)$.

4. Experimental estimation of the tunnelling barrier height in molecular junctions

Beebe *et al.* have reported a transition from direct tunnelling to Fowler-Nordheim tunnelling in molecular junctions[S9]. By measuring the transition voltage (V_{trans}), we can estimate the tunnelling barrier height that is given by the energy offset between the electrode Fermi energy (E_F) and the nearest molecular orbital (i.e., either HOMO or LUMO) responsible for the electronic conduction. When the applied bias is less than the barrier height (i.e., $V < \Phi_B/e$), direct tunnelling is assigned to the dominant transport mechanism in molecular junctions incorporating a family of alkyl and phenyl molecules[S10]. In the zero-bias limit, the barrier is assumed to be rectangular, and within the Simmons model[S11], the tunnelling current is approximated as $I \propto V \exp(-2d\sqrt{2m_e\Phi_B}/\hbar)$, where m_e is the electron effective mass, d is the barrier width (consistent with the molecular length), and h ($= 2\pi\hbar$) is the Planck's constant. At the opposite limit, when the applied bias exceeds the barrier height (i.e., $V > \Phi_B/e$), the barrier starts thinning at the Fermi energy, displaying a triangular barrier. Then, the conduction mechanism is replaced by Fowler-Nordheim tunnelling, or so-called field emission, and the $I(V)$ dependence for the triangular barrier is $I \propto V^2 \exp(-4d\sqrt{2m_e\Phi_B^3}/3\hbar qV)$. To compare charge transport in two distinct tunnelling regimes, it is useful to linearize the $I(V)$ curves in a logarithmic scale. For direct tunnelling, the $I(V)$ dependence is found to be

$$\ln\left(\frac{I}{V^2}\right) \propto \ln\left(\frac{1}{V}\right) - \frac{2d\sqrt{2m_e\Phi_B}}{\hbar} \qquad \text{(Eq. S1)}$$

Similarly, as to Fowler-Nordheim tunnelling, it scales as

$$\ln\left(\frac{I}{V^2}\right) \propto -\frac{4d\sqrt{2m_e\Phi_B^3}}{3\hbar q}\left(\frac{1}{V}\right) \qquad \text{(Eq. S2)}$$

It is obvious that a plot of $\ln(I/V^2)$ against $1/V$ displays a logarithmic growth for direct tunnelling (Eq. S1), whereas the plot indicates a linear relation for Fowler-Nordheim tunnelling (Eq. S2). Therefore, the transition from direct tunnelling to Fowler-Nordheim tunnelling will exhibit an inflection point on the plot of $\ln(I/V^2)$ against $1/V$ (as shown in Figs. 1b and 2b), which is consistent with a sequential change in the shape of the tunnelling barrier from a rectangular (V = 0 V) to a trapezoidal ($V < \Phi_B/e$) then to a triangular form ($V > \Phi_B/e$) upon the application of an increasing bias. Indeed, V_{trans} refers to the magnitude of the voltage required to permit a transition from rectangular to triangular barrier, and thus measuring V_{trans} provides a means of experimentally evaluating the height of the original rectangular barrier associated with the tunnelling transport in molecular junctions.

5. LUMO-mediated electron tunnelling through Au-BDCN-Au junction

Figure S8 below exhibits the transport characteristics of another molecule, specifically 1,4-benzenedicyanide (NC-C_6H_6-CN; denoted as BDCN). The reason this is of interest is that the LUMO level is closer to the electrode Fermi energy than the HOMO level. Whereas BDT is the analog of a p-type device (Fig. 2), this is analogous to an n-type device, which is in excellent agreement with a prior thermoelectric experiment[S12] and transmission calculation[S13]. Figure S8 shows the familiar Fowler-Nordheim plot [$\ln(I/V^2)$ versus $1/V$], which exhibits a now familiar dip at $V_{trans.}$ We also see the shift of V_{trans} with V_G. However, there is a fundamental difference between these BDCN characteristics and the BDT/ODT characteristics – in the BDCN case, V_{trans} shifts in the opposite direction. This is characteristics of n-type transport (dominated by the LUMO level), as it has been extensively illustrated[S14] in that the transition voltage in molecular junctions is dependent on electronic structure (i.e., the energy gap between the Fermi level and the nearest molecular orbital). The y intercept obtained from the plot of V_{trans} versus V_G indicates $V_{trans,0} = 1.69 \pm 0.05$ V, providing an estimate of $|E_F - E_{LUMO}|$ for the Au-BCDN-Au junction.

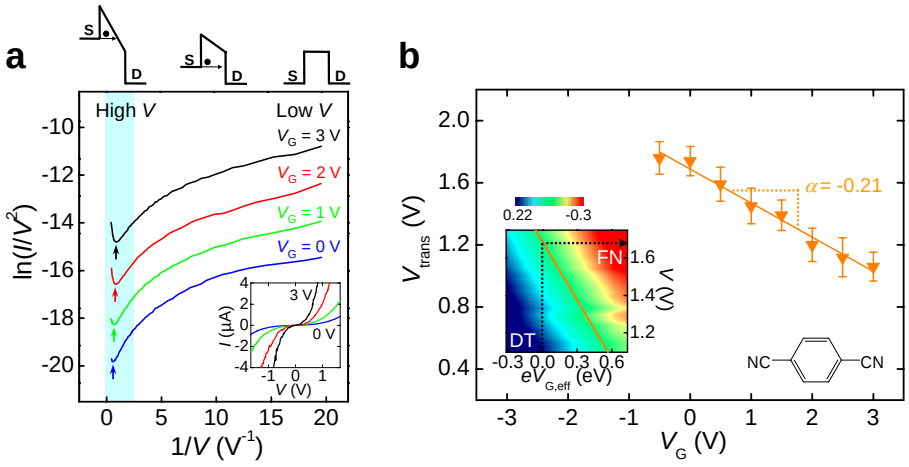

Figure S8. Gate-controlled charge transport characteristics of a Au-BDCN-Au junction. **a,** Fowler-Nordheim plots at gate voltages from 0 to 3 V with 1 V step, demonstrating the gate-variable transition from direct to Fowler-Nordheim tunnelling. The plots are offset vertically for clarity. Also shown are drawings of the barrier shape with the increasing bias. Inset shows $I(V)$ characteristics. **b,** Plot of V_{trans} versus V_G. Solid line indicates linear fit. Inset: the colour map of $d\ln(I/V^2)/d(1/V)$ (from Fowler–Nordheim plots) with linear fit (solid line) obtained from the plot of V_{trans} versus V_G. The zero-gate transition voltage is indicated by arrow. The negative value of α for Au-BDCN-Au junction indicates LUMO-mediated electron tunnelling (n-type like).

6. Vibrational mode assignments in IET spectra

Table S1. Summary of vibrational mode assignments in IET spectra for molecules investigated.

Molecule	Peak position		Vibrational mode[a]	Mode description	Refs
	mV	cm^{-1}			
ODT	27	218	ν(Au-S)	Au-S stretching	S15,S16,S17,S18
	86	694	ν(C-S)	C-S stretching	S15,S16,S17,S18,S19,S20
	113	911	$\delta_r(CH_2)$	CH_2 in-plane rocking	S15,S16,S17,S18,S21
	140	1129	ν(C-C)	C-C stretching	S15,S17,S18,S20,S21
	159	1282	$\gamma_w(CH_2)$	CH_2 out-of-plane wagging	S15,S16,S17,S18,S20,S21
	184	1483	$\delta_s(CH_2)$	CH_2 in-plane scissoring	S15,S17,S18
	357	2879	ν(C-H)	C-H stretching	S16,S17,S18,S19,S20,S21
BDT	26	210	ν(Au-S)	Au-S stretching	S15,S16,S17,S18
	95	766	γ(C-H)	Aryl C-H out-of-plane bending	S19,S20,S21
	138	1113	ν(18a)[b]	18a stretching ring mode	S19,S20,S21
	197	1589	ν(8a)[b]	8a stretching ring mode	S19,S20,S21

[a]To aid the assignments of the vibrational modes, the density functional theory (DFT) calculations were performed on the free thiolate form of ODT and BDT molecules at the B3LYP/6-311G** level using *Jaguar* v6.5 (Schrodinger Inc., Portland, OR, 2005). The calculated vibrational energies (frequencies) were scaled down by the factor of 0.962 to compare with the experimental results[S22]. For the detailed calculation results, see ref. S23.

[b]The benzene ring modes are given in terms of Wilson-Varsanyi terminology[S24].

7. Linewidth broadening in IET spectra of Au-BDT-Au junction

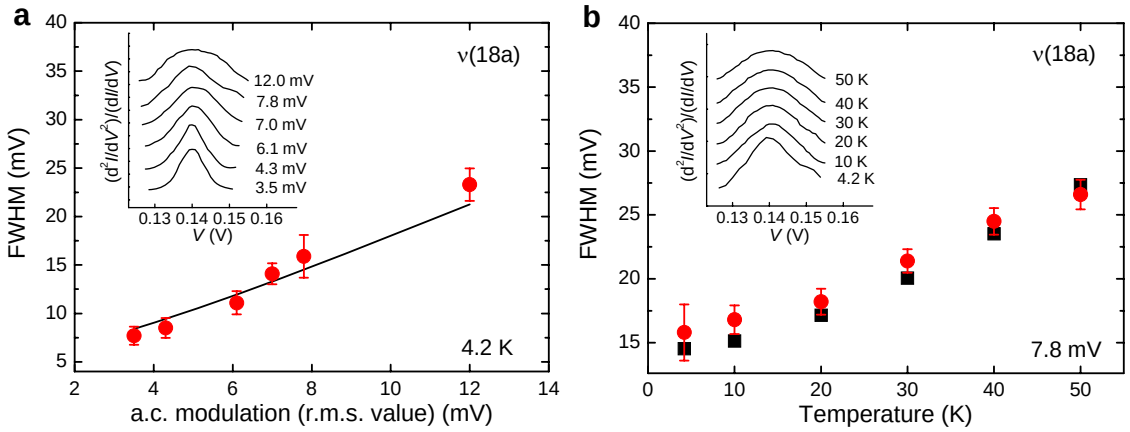

Figure S9. a, Linewidth broadening for the BDT ν(18a) mode as a function of a.c. modulation voltage at constant temperature (4.2 K). The circles indicate the experimental FWHM values of the ν(18a) peak. The intrinsic linewidth (W_I) is determined to be 5.60 ± 1.11 meV from a nonlinear least squares fit (solid line) to the modulation broadening data. Inset shows successive IET spectroscopy scans for the ν(18a) mode under increasing a.c. modulation voltage. **b,** Linewidth broadening for the BDT ν(18a) mode as a function of temperature at constant a.c. modulation voltage (7.8 mV). Inset shows successive IET spectroscopy scans for the ν(18a) mode under increasing temperature (4.2–50 K). There seems to be the good agreement between the experimental FWHM values (circles) and the theoretical linewidth values[S25] (squares) calculated by $[(5.4k_BT)^2 + (1.7V_{ac})^2 + (W_I)^2]^{1/2}$.

8. Projected density of states near HOMO levels of phenyl and alkyl molecules

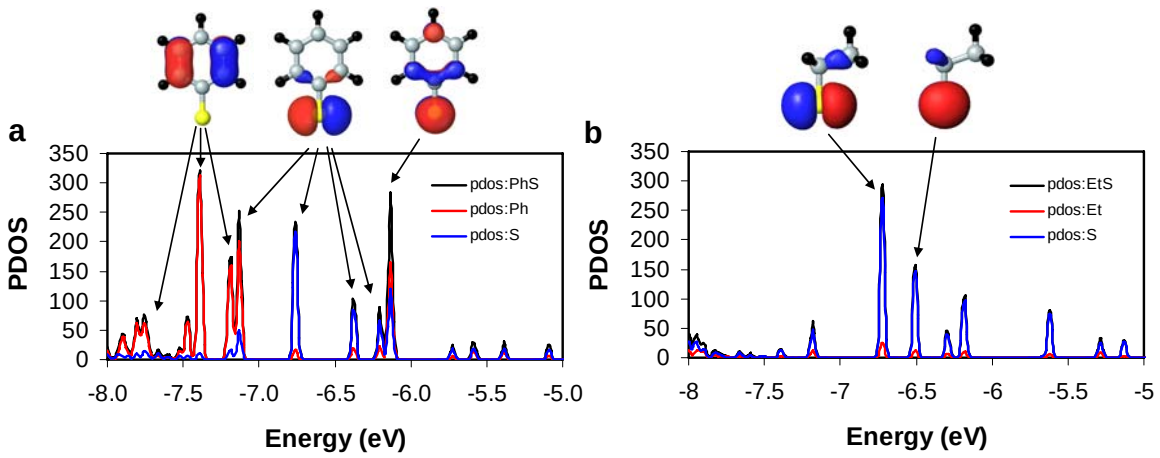

Figure S10. Projected density of states (PDOS) of the HOMO levels for PhS and EtS (Ph = phenyl; Et = ethyl) adsorbed on Au_{28} clusters, which were obtained from the DFT quantum mechanics calculations (B3LYP/LACVP**). Also are shown the isosurfaces of the HOMO levels corresponding to each peak of PDOS. The Au atoms were described using the Hay-Wadt small-core effective core potential with the outermost 19 electrons treated explicitly using the LACVP** basis set[S26]. The *Jaguar* v6.5 quantum chemistry software (Schrodinger Inc., Portland, OR, 2005) was used for all the calculations. **a,** The HOMO levels of PhS (especially near -6.1 and -7.2 eV) have significant contribution from the benzene ring (denoted by the red solid curve). The vibration modes associated with the benzene ring are enhanced by molecular orbital gating (Fig. 4a). **b,** The HOMO levels of EtS (between -6 and -8 eV) have essentially no contribution from the alkyl chain (denoted by the red solid curve). The vibration modes associated with the alkyl chain are nearly unchanged as varying $eV_{G,eff}$ (Fig. 3a).

9. Theoretical model on resonantly enhanced IET spectra

Persson and Baratoff[S27,S28] have developed a model using perturbation theory, describing IET process through a vibrating molecule chemisorbed on a metal surface, which highlights the implication of the resonant coupling between molecular orbitals and vibrational modes. According to this model, the manner in which the IET spectroscopy intensity and the line shape will be modified is described by equation (1) (in the main text). Depending on the position and width of the molecular resonance, the spectral intensity can be significantly enhanced and its line shape can be modified. Similarly, the numerical modeling results of Mii *et al*.[S29] and Galperin *et al*.[S30] have also showed the evolution of a IET spectroscopy feature from a peak to a peak-derivative to a dip as the position of the resonant level shifts.

Equation (1) contains the effect of the resonant coupling on both inelastic and elastic channels. The prefactor alone indicates the inelastic contribution to the total conductance proportional to the step function $\theta(eV - \Omega)$, while the terms in braces account for the corrections to the elastic channel, associated with two electron-phonon interaction events involving virtual phonon emission and reabsorption, which vary rapidly near the corresponding inelastic threshold, and then give rise to a singular contribution to the line shape and the intensity of IET spectra. Since the logarithmic term will only affect the line shape in equation (1), the relative change η in the normalised conductance across the threshold is given by the product of the prefactor and the first term in braces [S27,S28].

In light of equation (1), we are able to reproduce the experimental results for the gate-variable IET spectra of the BDT junction shown in Fig. 4a. Figure 4c shows the experimental values of η for the ν(18a) stretch mode at ~138 mV of the BDT junction

as a function of $eV_{G,eff}$. From the linear scaling of V_{trans} against V_G, we are able to estimate the position of the HOMO level. Thus, from equation (1) (neglecting the logarithmic term) by adjusting two parameters δE and Γ, a nonlinear least-squares fitting can be performed to fit the plot of η versus V_G. An excellent fit is obtained with δE = 0.21 ± 0.01 eV and Γ = 0.52 ± 0.02 eV, values that are in a reasonable range from a perusal of the IET spectroscopy literature[S27-S31]. With the best fitting parameters, the calculated values of η in terms of V_G are plotted as a solid curve in Fig. 4c. Using equation (1), we also fit the observed IET spectroscopy line shapes for various $eV_{G,eff}$. The results are shown in the inset of Fig. 4c where the spectra are centered in the proximity of the ν(18a) mode of the BDT junction. The simulated IET spectra for various $eV_{G,eff}$ are calculated by slightly broadening the step function and the logarithm in equation (1), keeping essentially the same $\delta E/\Gamma$ (previously obtained from fitting the plot of η vs. V_G).

References

S1. Love, J. C., Estroff, L. A., Kriebel, J. K., Nuzzo, R. G. & Whitesides, G. M. Self-Assembled Monolayers of Thiolates on Metals as a Form of Nanotechnology. *Chem. Rev.* **105**, 1103–1169 (2005).

S2. Park, H. *et al.* Fabrication of metallic electrodes with nanometer separation by electromigration. *Appl. Phys. Lett.* **75**, 301 (1999); Taychatanapat, T. *et al.* Imaging Electromigration during the Formation of Break Junctions. *Nano Lett.* **7**, 652 (2007); Strachan, D. R. *et al*. Controlled fabrication of nanogaps in ambient environment for molecular electronics. *Appl. Phys. Lett.* **86**, 043109 (2005).

S3. Strachan, D. R. *et al.* Clean electromigrated nanogaps imaged by transmission electron microscopy. *Nano Lett.* **6**, 441 (2006); Strachan, D. R. *et al.* Real-Time TEM Imaging of the Formation of Crystalline Nano-scale Gaps. *Phys. Rev. Lett.* **100**, 056805 (2008); Heersche, H. B. *et al.* In situ imaging of electromigration-induced nanogap formation by transmission electron microscopy. *Appl. Phys. Lett.* **91**, 72107 (2007).

S4. Park, J. *et al*. Coulomb blockade and the Kondo effect in single-atom transistors. *Nature* **417**, 722–725 (2002); Liang, W., Shores, M. P, Bockrath, M., Long, J. R. & Park, H. Kondo resonance in a single-molecule transistor. *Nature* **417**, 725–729 (2002).

S5. Cui, X. D. *et al.* Reproducible Measurement of Single-Molecule Conductivity. *Science* **294**, 571 (2001); Jang, S. Y. *et al.* Interpretation of Stochastic Events in Single Molecule Conductance Measurements. *Nano Lett.* **6**, 2362 (2006); Xu, B. *et al.* Measurement of Single-Molecule Resistance by Repeated Formation of Molecular Junctions. *Science* **301**, 1221 (2003); Xiao, X. Y. *et al.* Measurement of Single Molecule Conductance: Benzenedithiol and Benzenedimethanethiol. *Nano Lett*. **4**, 267 (2004); Lörtscher, E. *et al.* Statistical Approach to Investigating Transport through Single Molecules. *Phys. Rev. Lett.* **98**, 176807 (2007); Gonzalez, M. T. *et al.* Electrical Conductance of Molecular Junctions by a Robust Statistical Analysis. *Nano Lett.* **6**, 2238 (2006); Li, X. *et al.* Conductance of Single Alkanedithiols: Conduction Mechanism and Effect of Molecule-Electrode Contacts. *J. Am. Chem. Soc.* **128**, 2135(2006).

S6. Jang, S. Y. *et al.* Interpretation of Stochastic Events in Single Molecule Conductance Measurements. *Nano Lett.* **6**, 2362 (2006); Xu, B. *et al.* Measurement of Single-Molecule Resistance by Repeated Formation of Molecular Junctions. *Science* **301**, 1221 (2003); Wang, W. *et al.* Mechanism of Electron Conduction In

Self-Assembled Alkanethiol Monolayer Devices. *Phys. Rev. B* **68**, 035416 (2003); Li, X. *et al.* Conductance of Single Alkanedithiols: Conduction Mechanism and Effect of Molecule-Electrode Contacts. *J. Am. Chem. Soc.* **128**, 2135(2006); Cui, X. D. *et al.* Making electrical contacts to molecular monolayers. *Nanotechnology* **13**, 5 (2002); Engelkes, V. B. *et al.* Length-dependent transport in molecular junctions based on SAMs of alkanethiols and alkanedithiols: Effect of metal work function and applied bias on tunneling efficiency and contact resistance. *J. Am. Chem. Soc.* **126**, 14287 (2004); Holmlin, R. E. *et al.* Correlating electron transport and molecular structure in organic films. *Angew. Chem., Int. Ed.* **40**, 2316 (2001); Akkerman, H. B. *et al.* Towards molecular electronics with large-area molecular junctions. *Nature* **441**, 69 (2006).

S7. Galperin, M. *et al.* Nuclear Coupling and Polarization in Molecular Transport Junctions: Beyond Tunneling to Function. *Science* **319**, 1056 (2008); Wang, W. *et al.* Inelastic Electron Tunneling Spectroscopy of Alkanedithiol Self-Assembled Monolayers. *Nano Lett.* **4**, 643 (2004); Kushmerick, J. G. *et al.* Vibronic contributions to charge transport across molecular junctions. *Nano Lett*. **4**, 639 (2004); Long, D. P. *et al.* Effects of hydration on molecular junction transport. *Nat. Mater.* **5**, 901 (2006); Long, D. P. *et al.* Inelastic Electron Tunneling Spectroscopy of Alkane Monolayers with Dissimilar Attachment Chemistry to Gold. *J. Am. Chem. Soc.* **129**, 15303 (2007); Tal, O. *et al.* Electron-vibration interaction in single-molecule junctions: from contact to tunneling regime. *Phys. Rev. Lett.* **100**, 196804 (2008).

S8. Horowitz, P. & Hill, W. *The Art of Electronics* (Cambridge University Press, New York, 1989).

S9. Beebe, J. M., Kim, B., Gadzuk, J. W., Frisbie, C. D. & Kushmerick, J. G. Transition from direct tunneling to field emission in metal-molecule-metal junctions. *Phys. Rev. Lett.* **97**, 026801 (2006).

S10. Wang, W., Lee, T. & Reed, M. A. Mechanism of electron conduction in self-assembled alkanethiol monolayer devices. *Phys. Rev. B* **68**, 035416 (2003); Song, H., Lee, T., Choi, N.-J. & Lee, H. A statistical method for determining intrinsic electronic transport properties of self-assembled alkanethiol monolayer devices. *Appl. Phys. Lett.* **91**, 253116 (2007); Xu, B. & Tao, N. J. Measurement of single-molecule resistance by repeated formation of molecular junctions. *Science* **301**, 1221–1223 (2003); Wold, D. J., Haag, R., Rampi, M. A. & Frisbie, C. D. Distance dependence of electron tunneling through self-assembled monolayers measured by conducting probe atomic force microscopy: Unsaturated versus saturated

molecular junctions. *J. Phys. Chem. B* **106**, 2813–2816 (2002); Venkataraman, L., Klare, J. E., Nuckolls, C., Hybertsen, M. S. & Steigerwald, M. L. Dependence of single-molecule junction conductance on molecular conformation. *Nature* **442**, 904–907 (2006).

S11. Simmons, J. G. Generalized formula for the electric tunnel effect between similar electrodes separated by a thin insulating film. *J. Appl. Phys.* **34**, 1793–1803 (1963).

S12. Baheti, K. *et al.* Probing the Chemistry of Molecular Heterojunctions Using Thermoelectricity. *Nano Lett.* **8**, 715 (2008).

S13. Xue, Y. et al. End group effect on electrical transport through individual molecules: A microscopic study. *Phys. Rev. B*. **69**, 085403 (2004).

S14. Beebe, J. M. *et al.,* Transition from Direct Tunneling to Field Emission in Metal-Molecule-Metal Junctions. *Phys. Rev. Lett.* **97**, 026801 (2006); Beebe, J. M. *et al.* Measuring Relative Barrier Heights in Molecular Electronic Junctions with Ttransition Voltage Spectroscopy. *ACS Nano* **2**, 827 (2008); Zangmeister, C. D. *et al.* Controlling Charge-Carrier Type in Nanoscale Junctions with Linker Chemistry. *Small* **4**, 1143 (2008); Liu, K *et al.* Probing Charge Transport of Ruthenium-Complex-Based Molecular Wires at the Single-Molecule Level. *ACS Nano* **2**, 2315 (2008); Coll, M. *et al.* Formation of Silicon-Based Molecular Electronic Structures Using Flip-Chip Lamination. *J. Am. Chem. Soc.* **131**, 12451 (2009).

S15. Wang, W., Lee, T., Kretzschmar, I. & Reed, M. A. Inelastic electron tunneling spectroscopy of an alkanedithiol self-assembled monolayer. *Nano Lett.* **4**, 643–646 (2004).

S16. Zhang, X., McGill, S. A. & Xiong, P. Origin of the humidity sensitivity of Al/AlOx/MHA/Au molecular tunnel junctions. *J. Am. Chem. Soc.* **129**, 14470–14474 (2007).

S17. Long, D. P. & Troisi, A. Inelastic electron tunneling spectroscopy of alkane monolayers with dissimilar attachment chemistry to gold. *J. Am. Chem. Soc.* **129**, 15303–15310 (2007).

S18. Long, D. P. *et al.* Effects of hydration on molecular junction transport. *Nat. Mater.* **5**, 901–908 (2006).

S19. Yu, L. H., Zangmeister, C. D. & Kushmerick, J. G. Origin of discrepancies in inelastic electron tunneling spectra of molecular junctions. *Phys. Rev. Lett.* **98**, 206803 (2007).

S20. Beebe, J. M., Moore, H. J., Lee, T. R. & Kushmerick, J. G. Vibronic coupling in semifluorinated alkanethiol junctions: Implications for selection rules in inelastic electron tunneling spectroscopy. *Nano Lett.* **7**, 1364–1368 (2007).

S21. Kushmerick, J. G. *et al.* Vibronic contributions to charge transport across molecular junctions. *Nano Lett.* **4**, 639–642 (2004).

S22. Scott, A. P. & Radom, L. Harmonic vibrational frequencies: An evaluation of Hartree−Fock, Møller−Plesset, quadratic configuration interaction, density functional theory, and semiempirical scale factors. *J. Phys. Chem.* **100**, 16502-16513 (1996).

S23. Song, H. *et al.* Vibrational spectra of metal-molecule-metal junctions in electromigrated nanogap electrodes by inelastic electron tunneling. *Appl. Phys. Lett.* **94**, 103110 (2009).

S24. Varsanyi, G. *Assignments for Vibrational Spectra of Seven Hundred Benzene Derivatives* (John Wiley & Sons, New York, 1974).

S25. Lauhon, L. J. & Ho, W. Effects of temperature and other experimental variables on single molecule vibrational spectroscopy with the scanning tunneling microscope. *Rev. Sci. Instrum.* **72**, 216–223 (2001).

S26. Hay, P. J. & Wadt, W. R. Ab initio effective core potentials for molecular calculations. Potentials for K to Au including the outermost core orbitals. *J. Chem. Phys.* **82**, 299–310 (1985).

S27. Persson, B. N. J. & Baratoff, A. Inelastic electron tunneling from a metal tip: The contribution from resonant processes. *Phys. Rev. Lett.* **59**, 339–342 (1987).

S28. Baratoff, A. & Persson, B. N. J. Theory of the local tunneling spectrum of a vibrating adsorbate. *J. Vac. Sci. Technol. A* **6**, 331–355 (1988).

S29. Mii, T., Tikhodeev, S. G. & Ueba, H. Spectral features of inelastic electron transport via a localized state. *Phys. Rev. B* **68**, 205406 (2003).

S30. Galperin, M., Ratner, M. A. & Nitzan, A. On the line widths of vibrational features in inelastic electron tunneling spectroscopy. *Nano Lett.* **4**, 1605–1611 (2004).

S31. Komeda, T. Chemical identification and manipulation of molecules by vibrational excitation via inelastic tunneling process with scanning tunneling microscopy. *Prog. Surf. Sci.* **78,** 41–85 (2005).